Title: Preclinical assessment of Fibroblast Activation Protein-specific MRI as an alternative to PSMA for image-guided focal therapy of prostate cancer

Nicole Dmochowska[a*] PhD, Valentina Milanova[a*] PhD, Ramesh Mukkamala[b] PhD, Nguyen T.H. Pham[c] PhD, Madduri Srinivasarao[b] PhD, Lisa M. Ebert PhD[d] Timothy Stait-Gardner[e] PhD, Hien Le[f] MBBS, Anil Shetty[g] MD, Philip S. Low[b] PhD, Benjamin Thierry [a] PhD

[a]Future Industries Institute, University of South Australia, Adelaide, South Australia, Australia
[b]Department of Chemistry and Institute for Drug Discovery, Purdue University, West Lafayette, Indiana, United States
[c]Key Centre for Polymers and Colloids, School of Chemistry, The University of Sydney, Sydney, NSW, Australia
[d] Centre for Cancer Biology, University of South Australia and SA Pathology, Adelaide, South Australia, Australia
[e]Nanoscale Organisation and Dynamics Group, Western Sydney University, Sydney, New South Wales, Australia
[f]Department of Radiation Oncology, Royal Adelaide Hospital, Adelaide, SA, Australia
[g]Ferronova Pty Ltd, Mawson Lakes, SA, Australia

Corresponding author: Professor Benjamin Thierry, Bioengineering Lab, Future Industries Institute, MM Building, University of South Australia Mawson Lakes Campus, University Boulevard, Mawson Lakes, South Australia 5095, Australia, email: Benjamin.thierry@unisa.edu.au, telephone +618 830 23689.

Abstract

Accurate and precise delineation of gross tumour volumes remains a barrier to radiotherapy dose escalation and boost dosing in the treatment of solid tumours, such as prostate cancer. Magnetic resonance imaging of tumour molecular targets has the power to enable focal dose boosting, particularly when combined with technological advances such as MRI-LINAC. Fibroblast activation protein (FAP) is a transmembrane protein overexpressed in stromal components of >90% of epithelial carcinomas. Herein we compare targeted MRI of gold standard PSMA with FAP in the delineation of orthotopic tumours in a mouse model of prostate cancer. Control (no ligand), FAP and PSMA-targeting iron oxide nanoparticles were prepared with modification of an MRI agent (FerroTrace). Mice with orthotopic LNCaP tumours underwent T_2-weighted 3D MRI 24 hours after intravenous injection of contrast agents. FAP and PSMA nanoparticles produced contrast enhancement on MRI when compared to control nanoparticles, which was most pronounced on the tumour periphery. FAP-targeted MRI increased tumour contrast enhancement by ~15% when compared to PSMA. This study demonstrates preclinical feasibility of PSMA and FAP-targeted MRI which be used to enable targeted image-guided focal therapy of localized prostate cancer.

Background

Prostate cancer (PCa) is one of the most diagnosed malignancies in men (1) and, owing to its relatively high survival rate and frequent full gland treatment associated morbidity, is the leading cause of treatment–related years lived with disability worldwide. Along with radical prostatectomy, radiotherapy (RT) is a mainstay treatment option for all stages of disease, and is commonly delivered as a uniform dose over the entire prostate gland (2). There is mounting evidence that the risk of biochemical disease recurrence is reduced with dose escalation when greater than 80 Gy, especially in patients with intermediate or high-risk lesions. However, dose intensification of the whole gland is limited by off-target toxicities to adjacent organs at risk including the rectum, urethra, and bladder (3). Following pelvic radiotherapy, up to 30% of patients experience late grade III or IV genitourinary or gastrointestinal toxicities, with persistent long-term negative impacts on quality of life, through both mental and physical wellbeing, largely due to bowel disturbances(4, 5). Although modern RT techniques enable safer and more precise dose delivery to the prostate, treatment-associated morbidity remains a significant concern in the treatment of PCa patients.

PCa is a multifocal disease, often presenting with large primary intraprostatic lesions accompanied by smaller, well defined secondary lesions. Dominant intraprostatic lesions (index lesion) are considered to be the most aggressive, responsible for driving disease progression and prognosis, and are the most common sites of recurrence (6-8). Focal dose escalation RT approaches specifically target index lesions, balancing the risk of recurrence and patient's quality of life. For example, the recently reported FLAME study demonstrated that focal dose escalation under the guidance of multiparametric MRI (mpMRI) could improve biochemical recurrence free survival by 7%, without impacting morbidity and quality of life (9). Early results from a phase II trial investigating MRI-guided focused ultrasound ablation for localized intermediate risk PCa also demonstrated encouraging oncologic and functional outcomes with 93% of patients disease-free at 5 months after treatment (10). In a cohort of low to intermediate risk PCa, gadolinium enhanced MRI-guided focal laser ablation showed promising early oncologic results with 17% of participants requiring additional oncologic treatment after one year of initial treatment, with no significant side effects or impact to quality of life (11).

Target delineation, a key requirement to define gross tumour volumes (GTV) in intraprostatic focal treatment approaches, is commonly referred to as the Achilles' heel of RT. Owing to its superior soft-tissue resolution compared to computed tomography and the ability to acquire non-invasive functional imaging, mpMRI is rapidly becoming a staple tool in guiding PCa RT and more generally focal ablation. Adoption is supported by powerful technological advances such as the integration of MRI with linear accelerators (MRI-LINAC) and MRI-ultrasound (US) fusion set-ups that streamline intraoperative US image guidance with the resolution of MRI. However, mpMRI only has a moderate inter-rater agreement and is prone to a large false-positive rate and underestimation of tumour margins (12, 13). In addition, target delineation with mpMRI is not trivial, which substantially lengthens MRI-guided RT procedures and may

result in greater intrafraction motion. This is further limited by magnet strength and experience of the imaging team.

A recent study demonstrated increased consensus of prostate specific membrane antigen (PSMA)-PET volumes with histology compared with mpMRI for the delineation of intraprostatic GTVs, indicating that imaging with molecular targets increases imaging specificity (14). Furthermore, GTVs derived from mpMRI significantly underestimated true tumour volumes compared to PSMA-PET. For intraprostatic radiotherapy boosting, imaging of molecular targets such as PSMA may therefore advantageously replace or be used in addition to conventional mpMRI and provides additional biological characterisation of malignant tissue for dose planning. However, PSMA-PET can intrinsically lead to GTV underestimation due to various technical aspects such as partial volume effects limiting image resolution (15, 16). In addition, PET-based target delineation suffers from the absence of integrated systems such as MRI-LINAC and MRI-US fusion. Conceptually, molecular MRI should provide improved imaging of tumoural features on a biological level over what is to date conventionally afforded by PET imaging. However, despite very extensive research in molecular MRI, especially with nanoparticulate-based contrast agents, clinical translation is yet to be demonstrated. On the other hand, most of the related research has to date focussed on diagnostic applications as opposed to the feasibility of accurately imaging and delineating primary lesions.

Besides the imaging modality itself, a key requirement for molecular MRI is the selection of a biological target specific to the tumour. PSMA is often significantly overexpressed in PCa and as such has become the gold-standard target for molecular imaging of PCa (17). Multiple PSMA ligands are now available for PET imaging with various FDA and EMA-approved PSMA-targeting probes demonstrating success in the clinic. However, loss of PSMA expression has been known to occur in neuroendocrine, androgen receptor-negative PCa, reducing the efficacy of PSMA-targeting probes in these cases. Furthermore, 5-10% of primary PCa or primary PCa lesions are PSMA negative on PET (18, 19). Therefore, imaging of PSMA is not suitable for all patients, warranting the validation of additional imaging targets in PCa (20).

Fibroblast activation protein (FAP) is an extracellular serine protease that is upregulated in stromal components of >90% of epithelial tumours but with low or undetectable expression in normal tissues. In addition, FAP expression correlates with progression and worse prognosis (21, 22). Endothelial cells can also express FAP which contributes to the regulation of tumour angiogenesis, changes in capillary morphology and microvascular reorganization (23). Specifically, FAP has been found to be expressed by tumour endothelial cells during capillary formation but is absent in the mature endothelium (24). Additionally, FAP expression correlates with a significantly increased density of microvessels (25). As such, FAP is potentially a pan-cancer marker and a promising target for molecular imaging and therapy. FAP has been shown to be upregulated in PCa, and is predominantly expressed in cancer associated fibroblasts and reactive stromal cells adjacent to carcinoma cells (26-28). Recent studies demonstrated that in a population of patients with PSMA negative tumours, intermediate to high uptake of a ^{68}Ga-FAP inhibitor was observed in PCa (29, 30).

Furthermore, FAP-specific PET imaging of malignancies with low PSMA expression demonstrated more precise results when compared to PSMA-PET (31). Imaging of FAP in PCa has shown promise particularly in castrate resistant prostate cancer (CRPC), with elevated FAP expression also observed in neuroendocrine prostate cancer (NEPC) and patients undergoing neoadjuvant androgen deprivation therapy (ADT) (32).

To date, the utility and significance of FAP specific MRI is yet to be assessed. To address this question, here we report on benchmarking the performance of a FAP-targeted iron oxide nanoparticulate MRI agent against PSMA in the delineation of PCa in an orthotopic mouse model. Our experimental approach builds on a previously reported FAP-ligand designed by ligating fragments of existing FAP ligands that were identified by molecular docking studies to contribute most prominently to the specificity and affinity of FAP binding. The FAP and PSMA ligands were substituted from mannose in the FerroTrace maghemite nanoparticulate MRI agent that is presently undergoing clinical trialling as a lymphotropic contrast agent. Using this novel imaging platform, we demonstrate that FAP MRI yields superior tumour contrast and coverage compared to PSMA in a preclinical model of PCa.

Materials

The following chemicals were purchased and used as received without further purification. Trifluoroacetic acid, 1-Ethyl-3-(3-dimethylaminopropyl) carbodiimide hydrochloride (EDC.HCl), N-hydroxysuccinimide (NHS), 4-Morpholineethanesulfonic acid, 2-(N-Morpholino)ethanesulfonic acid hydrate (MES hydrate), 10X Phosphate Buffered Saline were purchased from Sigma Aldrich. Acetone and dichloromethane (DCM) we purchased from Chem-Supply. FAP binding ligand was synthesized as previously described (33). PSMA ligand Clu-CO-Lys-$(tBu)_3$ ester (CAS 1025796-31-9) was synthesized by Advanced Molecular Technologies (Scoresby, Victoria, Australia).

Analysis of FAP expression in PCa

To evaluate FAP expression in normal prostates and prostate adenocarcinoma, normalized FAP RNAseq (expected count-deseq2+1) data was obtained from the Therapeutically Applicable Research to Generate Effect Treatments initiative (TARGET)/the Cancer Genome Atlas (TCGA)/Genotype Tissue Expression (GTEx) dataset using the UCSC Xena platform (accessed 26/11/2021) (34). Corresponding patient prostate adenocarcinoma pathological T staging was obtained from the TCGA prostate adenocarcinoma (PRAD) data set (accessed 26/11/2021). Furthermore, immunohistochemistry staining of FAP in low- and high-grade prostate adenocarcinoma was obtained from the HPA059739 dataset deposited in the Human Protein Atlas (https://www.proteinatlas.org/ENSG00000078098-FAP/pathology/prostate+cancer#) (35).

Magnetic nanoparticle synthesis

The core maghemite iron oxide (γ-Fe_2O_3) nanoparticles were synthesised via coprecipitation of iron salts in aqueous solutions and subsequent controlled oxidation using iron nitrate as previously described (36). To achieve *in vivo* stability, the nanoparticles are colloidally stabilised by block copolymers synthesised using reversible addition-fragment chain-transfer (RAFT) polymerisation. The maghemite nanoparticles and RAFT block copolymer coating have been previously developed for the preparation of a lymphotropic MRI agent (FerroTrace, Ferronova) currently undergoing clinical trialling (36). Briefly, two types of block copolymer are attached to the nanoparticle surface: a stabilising-polymer (RAFT-5-MAPC2-15AAM-3PEO) and a targeting polymer with terminal FAP or PSMA ligands (RAFT-5MAPC2-70AAM-PSMA/FAP) in a mole ratio of 70% stabilising to 30% targeting.

Preparation of RAFT-5MAPC2-15AAM-3PEO

Polymers were prepared based on a previously published procedure with modifications (37). Methoxy triethylene glycol modified 2-{[butylsulfanyl)cabonothioyl]sulfanyl}propanoic acid (1.0 g), acrylamide (2.8 g), 4,4'-azobis(4-cyanovaleric acid) (0.050 g), dioxane (10 g) and water (10 g) were combined and dissolved before purging with nitrogen gas for 15 minutes and polymerising at 70°C for 2 hours. The mixture was allowed to cool, opened to air, then (methacryloyloxy)-ethyl]phosphonic acid (2.5 g) and 4,4'-azobis(4-cyanovaleric acid) (0.050 g) were added to the reaction mixture. The mixture was purged with nitrogen gas for 15 minutes, then heated at 70°C for 4 hours. The polymer was precipitated in acetone, repurified and collected by centrifugation.

Preparation of RAFT-5MAPC2-70AAM-PSMA/FAP polymers

RAFT-COOH (2-(((butylthio)carbonothioyl)-thio)-propanoic acid) (0.2 g), 4,4'-azobis(4-cyanovaleric acid) (0.012 g), acrylamide (4.17 g), dioxane (7.8 g) and water (12.1 g) were combined and dissolved. The reaction was magnetically stirred at 70°C for 4 hours in an inert atmosphere. The mixture was allowed to cool, opened to air and [2-(methacryloyloxy)-ethyl]phosphonic acid (0.81 g) and 4,4'-azobis(4-cyanovaleric acid) (0.012 g) were added to the reaction mixture. The reaction was purged with nitrogen gas for 15 minutes before heating to 70°C for 4 hours under magnetic stirring. At this step the RAFT-5MAPC2-70AAM polymer was precipitated in acetone, repurified, collected by centrifugation and stored prior to conjugation with the FAP and PSMA ligands.

For preparing RAFT-5MAPC2-70AAM-PSMA, the tert-butyl ester groups of the PSMA ligand [Clu-CO-Lys-$(tBu)_3$ ester] were first removed using 20% trifluoroacetic acid (TFA) in dichloromethane (DCM). Briefly, 20 mg/mL PSMA in 20% TFA in DCM was mixed for 3 hours at room temperature before vacuum drying. The residue was then dissolved in 10-20% aqueous acetic acid, transferred into a 50 mL falcon tube and a two-fold volume of chloroform was added. The reaction was mixed thoroughly before the layers were allowed to separate and the bottom organic layer containing the protective groups and non-volatile by-products was removed using a needle and syringe. The extraction of the aqueous layer was repeated

203 twice, and it was dried under high vacuum. The residue was dissolved in glacial acetic acid,
204 shell-freezed and lyophilized before use. The NH_2 derivatized FAP ligand was synthesized as
205 previously described and used for the preparation of the RAFT-5MAPC2-70AAM-FAP (31).

206 PSMA and FAP ligands were conjugated to the RAFT-5MAPC2-70AAM polymer using a
207 carbodiimide coupling reaction. First, 200 mg of poly[[(methacryloyloxy)-ethyl]phosphonic
208 acid]-*block*-poly(acrylamide), EDC.HCl (48 mg) and NHS (12 mg) were dissolved in 10 mL MES
209 buffer (pH 5.0 – 5.5). The solution was mixed in a sonic bath for 10 minutes and the activated
210 polymer was collected by precipitation in acetone followed by centrifugation. Second,
211 FAP/PSMA ligands (12 mg) were dissolved in 100 µL DMSO and diluted to a total volume of
212 10 mL with 10X PBS buffer prior to addition to the activated polymer. The reaction mixture
213 was stirred for 20 hours. The conjugated polymer was purified using centrifugal filters with a
214 3 kDa molecular weight cut off membrane. The product was diluted to a final concentration
215 of 50 mg/mL and stored at 4°C until further use.

216

217 **Preparation of PSMA and FAP nanoparticles**

218 17 mg of RAFT-5MAPC2-15AAM-3PEO and 20 mg of RAFT-5MAPC2-70AAM-PSMA/FAP
219 polymers were dissolved in 2 mL of water and the pH was adjusted to 4 using 0.1M NaOH.
220 The maghemite nanoparticles (45 mg as dried weight) were added to the polymer solution
221 under probe sonication. After mixing for 10 minutes, the pH was adjusted to 5.0 with NaOH
222 (0.1M). Sonication was continued for a total of 30 minutes and the pH was further adjusted
223 stepwise to 6.0 and 7.0. The nanoparticle suspension was purified using a centrifugal filter
224 with a 100 kDa molecular weight cut off membrane. Lastly, the nanoparticles were diluted
225 with 3% saline to obtain a final concentration of 30 mg Fe/mL in 0.9% saline. An illustration
226 of the PSMA/FAP nanoparticle preparation is shown in figure 1A. For the preparation of non-
227 targeted nanoparticles the method described above was repeated except RAFT-5MAPC2-
228 70AAM-PSMA/FAP was replaced by RAFT-5MAPC2-70AAM-COOH.

229

230 **Nanoparticle characterisation**

231 The morphology of the coated nanoparticles was studied using transmission electron
232 microscope (TEM; JEOL JEM-2100F-HR) equipped with a field emission gun operated at 200
233 kV. Images were recorded with a CCD Camera (Gatan Orius SC1000). Samples were prepared
234 by placing a small drop of sample suspension in water onto a 200-mesh carbon-coated copper
235 grid (ProSciTech) and subsequently evaporating the water in air.

236 Dynamic Light Scattering (DLS) data was recorded on a Malvern Instruments Zetasizer Nano
237 ZS at 25°C. The hydrodynamic size of all nanoparticles suspensions was measured at a
238 concentration of 0.1 mg Fe/mL and isotonic saline (0.9%) was used as suspending medium.
239 Measurement duration was chosen as automatic.

240 Surface zeta potential data was acquired using the same instrumentation. The Smoluchowski
241 method was used for the zeta potential measurements. The surface zeta potential of all

242 nanoparticle suspensions was measured at a concentration of 1 mg Fe/mL and 10mM saline
243 was used as the suspending medium.
244
245 **Cancer cell lines and culture conditions**
246 Cells were routinely cultured in RPMI-1640 medium (Gibco) supplemented with 10% fetal
247 bovine serum (FBS) (Gibco) and 1% penicillin/streptomycin (Gibco) in a humidified
248 atmosphere of 5% CO_2 at 37°C. The medium was replaced every 2-3 days and cells were split
249 once they reached 75-80% confluence using TrypLE Express (Gibco).
250
251 **Flow cytometric analysis of FAP expression in U87 and C32 cells**
252
253 Cells were harvested from flasks using TrypLE Select (Thermo Fisher), washed in PBS and
254 resuspended in FACS buffer (PBS + 1% bovine serum albumin (BSA) + 0.04% sodium azide).
255 Staining for FAP was performed using either a one- or two-step process. For one-step staining,
256 90 µl of cells were incubated with 10 µl of anti-FAP-PE (clone 427819; R&D Systems) for 20
257 minutes at room temperature before washing with FACS buffer. For two-step staining, cells
258 were incubated with mouse anti-FAP (clone 427819; R&D Systems) at a final concentration of
259 5µg/ml for 20 mininutes at room temperature and washed with FACS buffer, then incubated
260 with goat anti-mouse secondary antibody conjugated to AlexaFluor488 (Thermo Fisher #A-
261 11029) at 10 µg/ml for 20 minutes at room temperature, then washed again in FACS buffer.
262 Samples were acquired on an LSR Fortessa or Accuri C6 flow cytometer (both BD Biosciences).
263 Analysis was performed using FCS Express V7 Flow Research Edition (De Novo Software,
264 Pasadena, CA, USA).
265
266 **Magnetic nanoparticle *in vitro* binding assay**
267 To test the binding affinity of the PSMA/FAP nanoparticles, cellular uptake in cells expressing
268 the respective targets was measured *in vitro*. LNCaP cells were seeded in a T25 cell culture
269 flask at a density of 1 x 10^6 cells per flask. C32 cells were seeded in a 6 well plate at a density
270 of 3.5 x 10^5 cells per well in the complete cell culture medium as described above. The cells
271 were placed in a 37°C, 5% CO_2 incubator and allowed to adhere for 24 hours. PSMA, FAP and
272 control unconjugated nanoparticle suspensions were prepared at a concentration of 0.150
273 mg Fe/mL in cell culture medium. 6 mL of PSMA or control nanoparticle suspension was added
274 to each flask containing adherent LNCaP cells or 1 mL of FAP and control nanoparticle
275 suspension was added to each well containing adherent C32 cells. Three replicates were used
276 to test each of the nanoparticle formulations. Cells were incubated with the nanoparticle
277 suspensions for 24 hours in an incubator at 37°C in 5% CO_2 humidified atmosphere. After
278 incubation, cells were washed 3 times with PBS, detached using TrypLE Express and cell
279 pellets were collected via centrifugation at 500 g for 5 minutes. The cell pellets were washed
280 twice with PBS and were dried at 60°C overnight using a heating block. The dried cell pellets
281 were digested with trace metal grade nitric and hydrochloric acid (1:1 ratio by volume).

282 Digested samples were diluted with water to a total volume of 10 mL or 3 mL for LNCaP PSMA
283 nanoparticles and C32 FAP nanoparticle samples, respectively. Iron concentration was
284 measured by inductively coupled plasma mass spectroscopy (ICP-MS).
285
286 **Preclinical study in an orthotopic prostate cancer murine model**
287 All animal experiments were approved by the Animal Ethics Committee of the South
288 Australian Health and Medical Research Institute (SAHMRI) and were conducted in
289 accordance with Australian National Health and Medical Research Council (NHMRC)
290 guidelines and the Animal Welfare Act and conformed to the Australian Code for the Care and
291 Use of Animals for Scientific Purposes. Male NOD scid gamma (NSG) aged 6-8 weeks were
292 bred and group-housed in a specific pathogen free environment at the SAHMRI. Animals had
293 *ad libitum* access to food and water and were clinically assessed daily. Mice were humanely
294 euthanized via CO_2 inhalation to remove tissues.
295 Intraprostatic injection of cancer cells was performed as previously described (38). Briefly, a
296 lower midline incision was made, the bladder and prostate were externalised and 10 µL of
297 RPMI-1640 containing 1 x 10^6 LNCaP cells were injected into the anterior prostate using a
298 precooled Hamilton syringe. To analyse tumour engraftment and growth, mice underwent
299 weekly *in vivo* bioluminescence imaging (IVIS, Perkin Elmer), approximately 15-20 minutes
300 post intraperitoneal injection with 150 mg/kg D-luciferin potassium salt.
301
302 **Magnetic Resonance Imaging**
303 After 5-6 weeks of tumour growth, mice were intravenously injected with 40 mg Fe/kg
304 nanoparticles in up to 100 µL of saline. After a 24-hour uptake period, mice were
305 anaesthetised with 2% isoflurane in oxygen and were intraperitoneally injected with an
306 overdose of pentobarbital prior to transcardial perfusion with 4% paraformaldehyde. Mice
307 were postfixed in 4% paraformaldehyde prior to storage in PBS with 0.1% sodium azide. Mice
308 underwent *ex vivo* T2-weighted multiple graded echo sequence acquired using a 16.4T Bruker
309 Avance scanner (Bruker BioSpin, GmbH), with a 30 mm SAW coil (M2M Imaging, Brisbane,
310 Australia) (repetition time 40 ms, echo time 10 ms, number of averages 1, slice thickness 0.1
311 mm) or fast low angle shot (FLASH) sequence using 9.4T Bruker BioSpec scanner (Bruker
312 BioSpin, GmbH, repetition time 50 ms, echo time 10 ms, number of averages 1, slice thickness
313 0.1 mm). At the completion of scans, tumours were excised and underwent FLASH scans using
314 a 11.7T Bruker Avance II scanner (Bruker BioSpin, GmbH, repetition time 100 ms, echo time
315 5.34 ms, number of averages 10, slice thickness 0.2 mm). All imaging was performed at room
316 temperature. Horos was used to view scans (Horosproject.org, sponsored by Nimble Co LLC
317 d/b/a Purview in Annapolis, MD USA).
318 Calculations of proportions of black pixels were based on protocols previously reported (39,
319 40). In brief, three regions of interest (ROI) were manually drawn over the prostate tumours
320 in whole body MR scans using ImageJ software (Bethesda, Maryland, USA) (41). Pixel intensity

histograms were generated for each ROI. A low intensity pixel threshold value was set, based on the visual analysis of threshold peaks.

Histology and iron staining

After *ex vivo* MR imaging, excised tumours, spleens, kidneys and livers were mounted in paraffin and 4 µm thick sections were stained with hematoxylin and eosin (H&E) or Prussian blue using standard protocols. Images were processed using a Nanozoomer (Hamamatsu, Japan) and were visualized using ImageJ software (Bethesda, Maryland, USA).

Statistical analyses

Data are expressed as mean ± SEM in all cases. The significance of results were determined by unpaired t testing or one way ANOVA. Differences with a p value of less than 0.05 were considered to be statistically significant. The relationship between FAP expression and PSA levels and Gleason scores were assessed using simple linear regression.

Results

Human FAP expression in the normal prostate and prostate adenocarcinoma

Analysis of available transcriptomic data showed a significant increase in FAP expression from normal prostate to adenocarcinoma ($p<0.0001$) (figure 1a). Further analysis comparing the expression between pathological T stages demonstrated significant increases from normal prostate to early stage (I and II) ($p<0.0001$) and to locally advanced (stage III) ($p<0.0001$). However, there was no additional significant increase to advanced (IV) ($p>0.05$) (figure 1b). FAP expression was further demonstrated by FAP immunohistochemistry in biopsies of low- and high-grade prostate adenocarcinoma (figures 1e and f). Linear correlation of Gleason score with FAP expression showed a weak positive relationship ($R^2 = 0.072$) (figure 1c), whereas there was no correlation demonstrated with PSA ($R^2 = 0.005$) (figure 1d).

Characterization of magnetic nanoparticles

To assess the characteristics of the prepared PSMA and FAP nanoparticles, a set of physico-chemical characterisations were carried out. TEM images presented in figure 2b and c, taken at 60K x magnification, showed near spherical, evenly dispersed FAP and PSMA nanoparticles even when dried on a carbon film. DLS measurements of the hydrodynamic diameters confirmed that all of the coated nanoparticles have a narrow size distribution with an average hydrodynamic size of 60–65 nm when measured in physiological saline (figure 2d). All nanoparticles were also characterised with similar surface charge ranging from an average of -17 mV to -20 mV (figure 2e).

***In vitro* binding studies**

359 The binding affinities of the prepared PSMA/FAP nanoparticles to the PSMA and FAP
360 receptors were evaluated *in vitro* by comparing their cellular uptake in cancer cell lines which
361 overexpress the receptors of interest. For nanoparticles used in biomedical applications, it is
362 important to take into consideration the potential protein adsorption onto the nanoparticle's
363 surface which can impact the binding activity, also known as the protein corona (42, 43). For
364 taking the formation of the protein corona into account, cellular uptake studies were
365 performed in full cell culture media containing 10% serum and incubation time was prolonged
366 to a 24-hour period.

367 First, the binding activity of PSMA nanoparticles was tested in the PSMA expressing cell line
368 LNCaP (44). The results presented in figure 3b indicated that the non-targeted nanoparticles
369 had a much lower cellular uptake compared to the targeted PSMA nanoparticles. Similarly,
370 the binding activity of FAP nanoparticles was tested in the human melanoma cell line C32 as
371 the FAP receptor is expressed in melanoma cell lines (45). Flow cytometric analysis of FAP
372 expression demonstrated that C32 cells had approximately 25% greater proportion of FAP-
373 positive cells in contrast to U87 cells, which had been previously demonstrated to have high
374 levels of FAP expression (figure 3a). The targeted FAP nanoparticles had an uptake almost
375 twice as high as the non-targeted nanoparticles (figure 3c). Considering the similar
376 physicochemical features of the PSMA/FAP nanoparticles when compared with the
377 unconjugated control nanoparticles, these cellular uptake data validate the chemical design
378 and specific binding affinity of the conjugated nanoparticles to their respective targets.

379

380 **Magnetic resonance imaging of orthotopic prostate tumours**

381 There was a significant increase in tumour contrast enhancement on T_2-W whole body MRI
382 after administration of both PSMA nanoparticles and FAP nanoparticles in mice bearing
383 orthotopic LNCaP tumours compared to the unconjugated control nanoparticle group, as
384 quantitatively demonstrated by the proportions of intratumoural black pixels (figures 4 and
385 5, $p=0.0358$ for PSMA nanoparticles and $p<0.0001$ for FAP nanoparticles, n=3-4 per group).
386 FAP nanoparticle administration yielded ~15% improvement of tumour contrast
387 enhancement compared to PSMA nanoparticles ($p=0.0004$, n=4 per group). Administration of
388 non-targeted control nanoparticles resulted in a modest, nonsignificant increase in tumour
389 contrast relative to the no nanoparticle control group ($p=0.2615$, n=3 per group).

390

391 **Distribution of magnetic nanoparticles in tissues**

392 To examine the intratumoural distribution of non-heme iron after the administration of the
393 PSMA/FAP nanoparticles, Prussian blue staining was performed on sections of LNCaP
394 orthotopic prostate tumours and normal prostates (figure 6). No positive staining was
395 observed in normal prostate sections. The absence of Prussian blue staining in sections of
396 normal prostate for mice administrated with control, FAP and PSMA nanoparticles confirmed
397 the lack of significant nanoparticle accumulation in the absence of orthotopic tumours. LNCaP
398 tumours also showed minimal positive basal staining. In agreement with the MRI data,

399 modest Prussian blue staining was observed after administration of control nanoparticles. On
400 the other hand, LNCaP tumours showed significant positive staining after the administration
401 of PSMA and FAP nanoparticles, of which the staining was concentrated on the tumour
402 periphery. Both PSMA and FAP nanoparticles demonstrated heterogenous intermittent
403 intratumoural staining, some of which was suggestive of blood vessel staining, of which the
404 frequency was greater in FAP nanoparticles compared to PSMA nanoparticles.

405 To further assess the distribution of the iron oxide nanoparticles and their effect on MRI, high
406 resolution MR imaging of resected tumours treated with either FAP nanoparticles or PSMA
407 nanoparticles was performed. Preferential contrast enhancement was observed at the
408 tumour peripheries, in contrast to homogenous contrast enhancement throughout the
409 tumours (figure 7), suggesting preferential accumulation of the nanoparticles to the highly
410 vascularised tumour periphery, in qualitative agreement with the Prussian blue staining data.

411 Additionally, Prussian blue staining was performed to assess the distribution of iron oxide
412 nanoparticles in the kidney, liver and spleen in orthotopic tumour mice (figure 8). Through
413 visual assessment there was no increase in Prussian blue staining in the spleen and kidneys in
414 all nanoparticle groups when compared to the no particle control. As expected, we observed
415 a marginal increase in Prussian blue staining in the liver compared to the no nanoparticle
416 control, which was consistent among all nanoparticles. Furthermore, to preliminarily assess
417 potential acute toxicities, H&E staining was performed on the kidneys, liver and spleen of
418 LNCaP tumour bearing mice (figure 8). No changes in tissue morphology were observed across
419 the kidneys, liver and spleen in a control, PSMA and FAP-targeting nanoparticles, when
420 compared to the no nanoparticle control.

421

422 **Discussion**

423 Focal boost therapies of PCa aim to selectively eliminate dominant intraprostatic malignant
424 lesions whilst sparing surrounding off-target tissues, and in doing so achieving oncological
425 outcomes similar to those afforded by whole gland treatment but with reduced adverse
426 effects. To enable effective focal treatment with contemporary treatment approaches
427 including image guided RT, target volumes and safety margins must be precisely defined.
428 Current MRI techniques such as mpMRI have yielded promising performance in providing
429 treatment guidance but are susceptible to underestimation of the true tumour volume (46)
430 and are time and resource demanding. This may be improved through the utilisation of
431 molecular MRI targeting tumour markers.

432 Targeting of pan-cancer marker FAP has practise-redefining potential in the treatment of solid
433 tumours such as PCa, through improved boundary delineation, possibly enabling the use of
434 focal lesion ablative microboosts. FAP is predominantly expressed on cancer associated
435 fibroblasts (CAFs) which reside in the tumour stroma and expression is present in virtually all
436 solid tumours. In addition, unlike cancer cells, CAFs are not undergoing constant mutation,
437 adding to the promising targeting qualities of FAP (33, 47, 48). Prostate tumours can have
438 over 50% stromal component, which can be greater in cases of desmoplastic reaction (29). As
439 such, targeting of the tumour stroma may provide increased imaging sensitivity and contrast

agent retention at the intraprostatic target site compared with targeting of the tumour cells themselves. PCa metastases have also been demonstrated to be FAP positive, possibly enabling focal metastatic lesion ablative treatment, with further investigation required. In support of this train of thought, pilot studies using PSMA-PET have shown efficacy in image-guided radiotherapy of metastases for the treatment of oligorecurrent PCa (49). In another study, 1.5T MRI guided stereotactic body RT by LINAC guided by PSMA-PET produced encouraging oncological and tolerability results in the management of oligometastatic castration sensitive prostate cancer (50). Recently, FAP-targeted PET has demonstrated fair to good interobserver agreement rates in the detection of organ and lymph node metastases across a variety of tumour types (51). There are yet to be clinical studies investigating the use of molecular MRI contrast agents in image-guided RT. FAP-targeted MRI-guided radiotherapy may also prove beneficial in palliative radiotherapy, particularly in reducing pain arising from PCa bone metastases, leading to improved quality of life (52).

FAP-specific imaging may be most beneficial in late stage and clinically aggressive cancers, in which FAP expression can be more pronounced than PSMA and in cases with doubtful lesions, therapy failure and/or PSMA downregulation or negative disease (31, 53). Patients undergoing long-term ADT may have a decreased detection sensitivity on PSMA imaging due to downregulation of the receptor, although this issue may be mitigated by ceasing ADT prior to imaging studies (54). Current literature suggests that short-term ADT upregulates PSMA, suggesting that PSMA-targeted imaging is suitable in these patients.

Although various FAP and PSMA-specific PET tracers are being actively developed, PET imaging lacks the resolution that is optimal for focal radiotherapy. MR boasts superior soft tissue contrast, visualization of organ movement and the ability to monitor changes in tumour and tissue physiology, enabling improved adaptation of target volumes between RT treatment fractions (55). However, interpretation of PCa mpMRI is susceptible to significant interpretation variability as demonstrated by discordance in prostate imaging reporting and data system (PIRADS) score assignment and cancer yield by radiologists (56). MRI provides high resolution 3D morphological information which can be enhanced with the use of magnetic core nanoparticles which cause hypointense signals (darkening) on MR imaging by decreasing the relaxation times of protons in surrounding water molecules. This exogenous contrast of the tumour may lead to decreased inter-observer variability of GTV delineation. The utilisation of FAP or PSMA-targeted MRI may also improve the delineation of low-grade disease, such as Gleason 3+3 cancers which are often missed on MRI (57). Furthermore, it was found that T2-weighted MRI underestimated GTVs, longest axis and pathological tumour extent in nearly every case. Furthermore, cellular composition, density and interstitial stromal space have an effect on diffusion-weighted imaging (DWI) and derived apparent diffusion coefficient (ADC) maps, which may contribute towards the underestimation of GTVs (58).

In this study we designed, synthesized and characterized FAP and PSMA targeted iron oxide nanoparticles for molecular MRI and comparatively assessed imaging performance *in vivo* in an orthotopic model of prostate cancer. To our knowledge, this is the first report describing the use of FAP specific MRI. The ligand targeted nanoparticles are modified from a

lymphotropic agent that has been validated in a large animal model and presently undergoing clinical trial (ACTRN12620000831987). This design relies on targeting and stabilising block copolymers of different lengths that enable efficient targeting using small molecule ligands as shown in the excellent binding affinity observed here *in vitro* with PSMA and FAP expressing cells.

Both FAP and PSMA targeted nanoparticles yielded improved tumour accumulation as shown by increase in MRI contrast in orthotopic tumour bearing mice compared to non-targeted nanoparticles. It is noteworthy that FAP-targeted MRI outperformed MRI targeting PSMA, the current clinical imaging benchmark, in contrast enhancement and delineation of prostate tumours in the orthotopic mouse model used here. The LNCaP tumour model was selected for this study as it commonly used for preclinical studies of PSMA specific diagnostic and therapeutic agents. Additionally, the expression of FAP in the stroma of orthotopic LNCaP tumours has been previously demonstrated as indicated by colocalization of both FAP and a-smooth muscle actin (59). The excellent imaging performance of the FAP nanoparticles observed here could be explained by the distribution of FAP expression, which predominantly occurs in the stroma and vasculature, and might therefore be more accessible to nanoparticulate imaging agents than markers expressed by tumour cells. Not surprisingly, the enhanced contrast associated to the presence of the iron oxide nanoparticles was found to be more pronounced at the periphery of the orthotopic tumours. This can be explained by the higher density of vascular structures at the periphery of such orthotopic models (60). As expected, unconjugated nanoparticles provided a modest improvement in the MRI contrast. Non-specific accumulation of nanoparticles within solid tumours is typically observed in preclinical mice models, although the precise mechanisms are still controversial (61). Enhanced tumour contrast on MRI has also been confirmed in several clinical trials for various dextran-coated iron oxide nanoparticles (62). The ongoing NCT04682847 trial investigates the use of Ferumoxytol, a non-targeted iron oxide nanoparticle, in MRI-LINAC treatment of hepatic cancer.

Considering the pan-cancer nature of FAP expression in the stroma of solid tumours, FAP-specific MRI with rationally designed iron oxide nanoparticles may prove useful in the delineation of other solid tumours such as gastrointestinal and brain cancer. In the future, FAP specific MRI may also be useful to guide RT with proton therapies, thereby fully harnessing the uniquely precise dose deposition afforded by this technique (63).

Disclosures

ND, VM, RM, PL and BT hold patents for FAP imaging technologies. BT is a founding member and shareholder of Ferronova Pty Ltd. ND and VM salaries are funded through Australian National Health and Medical Research Council grant 1158-755 and each undertake duties involving research and development that contribute to Ferronova Pty Ltd. AS is an employee of Ferronova Pty Ltd.

Funding

This research was supported by funding from an Australian National Health and Medical Research Council grant number 1158-755 (BT as chief investigator A).

Acknowledgements

We acknowledge the facilities and scientific and technical assistance of the National Imaging Facility, a National Collaborative Research Infrastructure Strategy (NCRIS) capability, at SAHMRI PIRL, the University of Western Sydney and the University of Queensland.

CRediT author statement

Nicole Dmochowska: conceptualization, methodology, validation, formal analysis, investigation, resources, data curation, writing -original draft, writing – review & editing, visualization, project administration. **Valentina Milanova:** conceptualization, methodology, validation, formal analysis, investigation, resources, data curation, writing – original draft, writing – review & editing. **Ramesh Mukkamala:** resources, writing – review & editing. **Nguyen T. H. Pham:** methodology, validation, investigation, resources, data curation. **Madduri Srinivasarao:** resources, writing – review & editing. **Lisa Ebert:** methodology, validation, formal analysis, investigation, data curation, writing – review & editing. **Timothy Stait-Gardner:** resources, data curation, writing – review & editing. **Hien Le:** writing – review & editing. **Anil Shetty:** methodology, writing – review & editing. **Phil Low:** resources, writing – review & editing, funding acquisition. **Benjamin Thierry:** conceptualization, methodology, resources, writing – original draft, writing – review & editing, visualization, supervision, project administration, funding acquisition.

References

1.Sung H, Ferlay J, Siegel RL, Laversanne M, Soerjomataram I, Jemal A, et al. Global Cancer Statistics 2020: GLOBOCAN Estimates of Incidence and Mortality Worldwide for 36 Cancers in 185 Countries. *CA Cancer J Clin* 2021;**71**:209-49.

2.Goodman CD, Fakir H, Pautler S, Chin J, Bauman GS. Dosimetric Evaluation of PSMA PET-Delineated Dominant Intraprostatic Lesion Simultaneous Infield Boosts. *Adv Radiat Oncol* 2020;**5**:212-20.

3.Viani GA, Stefano EJ, Afonso SL. Higher-than-conventional radiation doses in localized prostate cancer treatment: a meta-analysis of randomized, controlled trials. *Int J Radiat Oncol Biol Phys* 2009;**74**:1405-18.

4.Mazariego CG, Egger S, King MT, Juraskova I, Woo H, Berry M, et al. Fifteen year quality of life outcomes in men with localised prostate cancer: population based Australian prospective study. *BMJ* 2020;**371**:m3503.

5.Matta R, Chapple CR, Fisch M, Heidenreich A, Herschorn S, Kodama RT, et al. Pelvic Complications After Prostate Cancer Radiation Therapy and Their Management: An International Collaborative Narrative Review. *Eur Urol* 2019;**75**:464-76.

6.Arrayeh E, Westphalen AC, Kurhanewicz J, Roach M, 3rd, Jung AJ, Carroll PR, et al. Does local recurrence of prostate cancer after radiation therapy occur at the site of primary tumor? Results of a longitudinal MRI and MRSI study. *Int J Radiat Oncol Biol Phys* 2012;**82**:e787-93.

7.Pucar D, Hricak H, Shukla-Dave A, Kuroiwa K, Drobnjak M, Eastham J, et al. Clinically significant prostate cancer local recurrence after radiation therapy occurs at the site of primary tumor: magnetic resonance imaging and step-section pathology evidence. *Int J Radiat Oncol Biol Phys* 2007;**69**:62-9.

8.Murray JR, Tree AC, Alexander EJ, Sohaib A, Hazell S, Thomas K, et al. Standard and Hypofractionated Dose Escalation to Intraprostatic Tumor Nodules in Localized Prostate Cancer: Efficacy and Toxicity in the DELINEATE Trial. *Int J Radiat Oncol Biol Phys* 2020;**106**:715-24.

9.Kerkmeijer LGW, Groen VH, Pos FJ, Haustermans K, Monninkhof EM, Smeenk RJ, et al. Focal Boost to the Intraprostatic Tumor in External Beam Radiotherapy for Patients With Localized Prostate Cancer: Results From the FLAME Randomized Phase III Trial. *J Clin Oncol* 2021;**39**:787-96.

10.Ghai S, Finelli A, Corr K, Chan R, Jokhu S, Li X, et al. MRI-guided Focused Ultrasound Ablation for Localized Intermediate-Risk Prostate Cancer: Early Results of a Phase II Trial. *Radiology* 2021;**298**:695-703.

599 11.Walser E, Nance A, Ynalvez L, Yong S, Aoughsten JS, Eyzaguirre EJ, et al. Focal Laser Ablation
600 of Prostate Cancer: Results in 120 Patients with Low- to Intermediate-Risk Disease. *J Vasc*
601 *Interv Radiol* 2019;**30**:401-9 e2.

602 12.Muller BG, Shih JH, Sankineni S, Marko J, Rais-Bahrami S, George AK, et al. Prostate Cancer:
603 Interobserver Agreement and Accuracy with the Revised Prostate Imaging Reporting and Data
604 System at Multiparametric MR Imaging. *Radiology* 2015;**277**:741-50.

605 13.Ahmed HU, El-Shater Bosaily A, Brown LC, Gabe R, Kaplan R, Parmar MK, et al. Diagnostic
606 accuracy of multi-parametric MRI and TRUS biopsy in prostate cancer (PROMIS): a paired
607 validating confirmatory study. *Lancet* 2017;**389**:815-22.

608 14.Bettermann AS, Zamboglou C, Kiefer S, Jilg CA, Spohn S, Kranz-Rudolph J, et al. [(68)Ga-
609]PSMA-11 PET/CT and multiparametric MRI for gross tumor volume delineation in a slice by
610 slice analysis with whole mount histopathology as a reference standard - Implications for focal
611 radiotherapy planning in primary prostate cancer. *Radiother Oncol* 2019;**141**:214-9.

612 15.Piert M, Shankar PR, Montgomery J, Kunju LP, Rogers V, Siddiqui J, et al. Accuracy of tumor
613 segmentation from multi-parametric prostate MRI and (18)F-choline PET/CT for focal
614 prostate cancer therapy applications. *EJNMMI Res* 2018;**8**:23.

615 16.Piert M, Park H, Khan A, Siddiqui J, Hussain H, Chenevert T, et al. Detection of aggressive
616 primary prostate cancer with 11C-choline PET/CT using multimodality fusion techniques. *J*
617 *Nucl Med* 2009;**50**:1585-93.

618 17.Bouchelouche K, Choyke PL, Capala J. Prostate specific membrane antigen- a target for
619 imaging and therapy with radionuclides. *Discov Med* 2010;**9**:55-61.

620 18.Budaus L, Leyh-Bannurah SR, Salomon G, Michl U, Heinzer H, Huland H, et al. Initial
621 Experience of (68)Ga-PSMA PET/CT Imaging in High-risk Prostate Cancer Patients Prior to
622 Radical Prostatectomy. *Eur Urol* 2016;**69**:393-6.

623 19.Maurer T, Gschwend JE, Rauscher I, Souvatzoglou M, Haller B, Weirich G, et al. Diagnostic
624 Efficacy of (68)Gallium-PSMA Positron Emission Tomography Compared to Conventional
625 Imaging for Lymph Node Staging of 130 Consecutive Patients with Intermediate to High Risk
626 Prostate Cancer. *J Urol* 2016;**195**:1436-43.

627 20.Tosoian JJ, Gorin MA, Rowe SP, Andreas D, Szabo Z, Pienta KJ, et al. Correlation of PSMA-
628 Targeted (18)F-DCFPyL PET/CT Findings With Immunohistochemical and Genomic Data in a
629 Patient With Metastatic Neuroendocrine Prostate Cancer. *Clin Genitourin Cancer*
630 2017;**15**:e65-e8.

631 21.Zi F, He J, He D, Li Y, Yang L, Cai Z. Fibroblast activation protein alpha in tumor
632 microenvironment: recent progression and implications (review). *Mol Med Rep*
633 2015;**11**:3203-11.

634 22.Liu F, Qi L, Liu B, Liu J, Zhang H, Che D, et al. Fibroblast activation protein overexpression
635 and clinical implications in solid tumors: a meta-analysis. *PLoS One* 2015;**10**:e0116683.

636 23.Aimes RT, Zijlstra A, Hooper JD, Ogbourne SM, Sit ML, Fuchs S, et al. Endothelial cell serine
637 proteases expressed during vascular morphogenesis and angiogenesis. *Thromb Haemost*
638 2003;**89**:561-72.

639 24.Xin L, Gao J, Zheng Z, Chen Y, Lv S, Zhao Z, et al. Fibroblast Activation Protein-α as a Target
640 in the Bench-to-Bedside Diagnosis and Treatment of Tumors: A Narrative Review. *Frontiers in*
641 *Oncology* 2021;**11**.

642 25.Gao LM, Wang F, Zheng Y, Fu ZZ, Zheng L, Chen LL. Roles of Fibroblast Activation Protein
643 and Hepatocyte Growth Factor Expressions in Angiogenesis and Metastasis of Gastric Cancer.
644 *Pathol Oncol Res* 2019;**25**:369-76.

645 26.Giannoni E, Bianchini F, Masieri L, Serni S, Torre E, Calorini L, et al. Reciprocal activation of
646 prostate cancer cells and cancer-associated fibroblasts stimulates epithelial-mesenchymal
647 transition and cancer stemness. *Cancer Res* 2010;**70**:6945-56.

648 27.LeBeau AM, Brennen WN, Aggarwal S, Denmeade SR. Targeting the cancer stroma with a
649 fibroblast activation protein-activated promelittin protoxin. *Mol Cancer Ther* 2009;**8**:1378-86.

650 28.Tuxhorn JA, Ayala GE, Smith MJ, Smith VC, Dang TD, Rowley DR. Reactive stroma in human
651 prostate cancer: induction of myofibroblast phenotype and extracellular matrix remodeling.
652 *Clin Cancer Res* 2002;**8**:2912-23.

653 29.Hintz HM, Gallant JP, Vander Griend DJ, Coleman IM, Nelson PS, LeBeau AM. Imaging
654 Fibroblast Activation Protein Alpha Improves Diagnosis of Metastatic Prostate Cancer with
655 Positron Emission Tomography. *Clin Cancer Res* 2020;**26**:4882-91.

656 30.Khreish F, Rosar F, Kratochwil C, Giesel FL, Haberkorn U, Ezziddin S. Positive FAPI-PET/CT
657 in a metastatic castration-resistant prostate cancer patient with PSMA-negative/FDG-positive
658 disease. *Eur J Nucl Med Mol Imaging* 2020;**47**:2040-1.

659 31.Kessel K, Seifert R, Weckesser M, Boegemann M, Huss S, Kratochwil C, et al. Prostate-
660 specific membrane antigen and fibroblast activation protein distribution in prostate cancer:
661 preliminary data on immunohistochemistry and PET imaging. *Ann Nucl Med* 2022;**36**:293-301.

662 32.Kesch C, Yirga L, Dendl K, Handke A, Darr C, Krafft U, et al. High fibroblast-activation-
663 protein expression in castration-resistant prostate cancer supports the use of FAPI-molecular
664 theranostics. *Eur J Nucl Med Mol Imaging* 2021;**49**:385-9.

665 33.Roy J, Hettiarachchi SU, Kaake M, Mukkamala R, Low PS. Design and validation of fibroblast
666 activation protein alpha targeted imaging and therapeutic agents. *Theranostics*
667 2020;**10**:5778-89.

668 34.Goldman MJ, Craft B, Hastie M, Repecka K, McDade F, Kamath A, et al. Visualizing and
669 interpreting cancer genomics data via the Xena platform. *Nat Biotechnol* 2020;**38**:675-8.

670 35.Uhlen M, Fagerberg L, Hallstrom BM, Lindskog C, Oksvold P, Mardinoglu A, et al.
671 Proteomics. Tissue-based map of the human proteome. *Science* 2015;**347**:1260419.

672 36.Krishnan G, Cousins A, Pham N, Milanova V, Nelson M, Krishnan S, et al. Preclinical
673 evaluation of a mannose-labeled magnetic tracer for enhanced sentinel lymph node retention
674 in the head and neck. *Nanomedicine* 2022:102546.

675 37.Bryce NS, Pham BTT, Fong NWS, Jain N, Pan EH, Whan RM, et al. The composition and end-
676 group functionality of sterically stabilized nanoparticles enhances the effectiveness of co-
677 administered cytotoxins. *Biomater Sci* 2013;**1**:1260-72.

678 38.Linxweiler J, Korbel C, Muller A, Hammer M, Veith C, Bohle RM, et al. A novel mouse model
679 of human prostate cancer to study intraprostatic tumor growth and the development of
680 lymph node metastases. *Prostate* 2018;**78**:664-75.

681 39.Ngen EJ, Benham Azad B, Boinapally S, Lisok A, Brummet M, Jacob D, et al. MRI Assessment
682 of Prostate-Specific Membrane Antigen (PSMA) Targeting by a PSMA-Targeted Magnetic
683 Nanoparticle: Potential for Image-Guided Therapy. *Mol Pharm* 2019;**16**:2060-8.

684 40.Ngen EJ, Chen Y, Azad BB, Boinapally S, Jacob D, Lisok A, et al. Prostate-specific membrane
685 antigen (PSMA)-targeted photodynamic therapy enhances the delivery of PSMA-targeted
686 magnetic nanoparticles to PSMA-expressing prostate tumors. *Nanotheranostics* 2021;**5**:182-
687 96.

688 41.Schneider CA, Rasband WS, Eliceiri KW. NIH Image to ImageJ: 25 years of image analysis.
689 *Nat Methods* 2012;**9**:671-5.

690 42.Amstad E, Textor M, Reimhult E. Stabilization and functionalization of iron oxide
691 nanoparticles for biomedical applications. *Nanoscale* 2011;**3**:2819-43.

692 43.Oh JY, Kim HS, Palanikumar L, Go EM, Jana B, Park SA, et al. Cloaking nanoparticles with
693 protein corona shield for targeted drug delivery. *Nat Commun* 2018;**9**:4548.

694 44.Ben Jemaa A, Sallami S, Ceraline J, Oueslati R. A novel regulation of PSMA and PSA
695 expression by Q640X AR in 22Rv1 and LNCaP prostate cancer cells. *Cell Biol Int* 2013;**37**:464-
696 70.

697 45.Tyulkina DV, Pleshkan VV, Alekseenko IV, Kopantseva MR, Sverdlov ED. Expression of the
698 FAP gene in non-fibroblast human cell lines. Development of cancer-associated fibroblast
699 models. *Dokl Biochem Biophys* 2016;**470**:319-21.

700 46.Wysock JS, Lepor H. Multi-parametric MRI imaging of the prostate-implications for focal
701 therapy. *Transl Androl Urol* 2017;**6**:453-63.

702 47.Tao L, Huang G, Song H, Chen Y, Chen L. Cancer associated fibroblasts: An essential role in
703 the tumor microenvironment. *Oncol Lett* 2017;**14**:2611-20.

704 48.Du H, Che G. Genetic alterations and epigenetic alterations of cancer-associated
705 fibroblasts. *Oncol Lett* 2017;**13**:3-12.

706 49.Stefan AK, Katharina S, Clemens K, Erik W, Matthias FH, Sonja K, et al. Clinical outcome of
707 PSMA-guided radiotherapy for patients with oligorecurrent prostate cancer. *Eur J Nucl Med*
708 *Mol Imaging* 2021;**48**:143-51.

709 50.Mazzola R, Cuccia F, Figlia V, Rigo M, Nicosia L, Giaj-Levra N, et al. Stereotactic body
710 radiotherapy for oligometastatic castration sensitive prostate cancer using 1.5 T MRI-Linac:
711 preliminary data on feasibility and acute patient-reported outcomes. *Radiol Med*
712 2021;**126**:989-97.

713 51.Serfling SE, Hartrampf PE, Zhi Y, Higuchi T, Rowe SP, Bundschuh L, et al. Interobserver
714 Agreement Rates on Fibroblast Activation Protein Inhibitor-Directed Molecular Imaging and
715 Therapy. *Clin Nucl Med* 2022.

716 52.De Felice F, Piccioli A, Musio D, Tombolini V. The role of radiation therapy in bone
717 metastases management. *Oncotarget* 2017;**8**:25691-9.

718 53.Isik EG, Has-Simsek D, Sanli O, Sanli Y, Kuyumcu S. Fibroblast Activation Protein-Targeted
719 PET Imaging of Metastatic Castration-Resistant Prostate Cancer Compared With 68Ga-PSMA
720 and 18F-FDG PET/CT. *Clin Nucl Med* 2022;**47**:e54-e5.

721 54.Vaz S, Hadaschik B, Gabriel M, Herrmann K, Eiber M, Costa D. Influence of androgen
722 deprivation therapy on PSMA expression and PSMA-ligand PET imaging of prostate cancer
723 patients. *Eur J Nucl Med Mol Imaging* 2020;**47**:9-15.

724 55.Otazo R, Lambin P, Pignol JP, Ladd ME, Schlemmer HP, Baumann M, et al. MRI-guided
725 Radiation Therapy: An Emerging Paradigm in Adaptive Radiation Oncology. *Radiology*
726 2021;**298**:248-60.

56.Sonn GA, Fan RE, Ghanouni P, Wang NN, Brooks JD, Loening AM, et al. Prostate Magnetic Resonance Imaging Interpretation Varies Substantially Across Radiologists. *Eur Urol Focus* 2019;**5**:592-9.

57.Priester A, Natarajan S, Khoshnoodi P, Margolis DJ, Raman SS, Reiter RE, et al. Magnetic Resonance Imaging Underestimation of Prostate Cancer Geometry: Use of Patient Specific Molds to Correlate Images with Whole Mount Pathology. *J Urol* 2017;**197**:320-6.

58.Hectors SJ, Semaan S, Song C, Lewis S, Haines GK, Tewari A, et al. Advanced Diffusion-weighted Imaging Modeling for Prostate Cancer Characterization: Correlation with Quantitative Histopathologic Tumor Tissue Composition-A Hypothesis-generating Study. *Radiology* 2018;**286**:918-28.

59.Brennen WN, Rosen DM, Wang H, Isaacs JT, Denmeade SR. Targeting carcinoma-associated fibroblasts within the tumor stroma with a fibroblast activation protein-activated prodrug. *J Natl Cancer Inst* 2012;**104**:1320-34.

60.Liu W, Zhu Y, Ye L, Zhu Y, Wang Y. Comparison of tumor angiogenesis in subcutaneous and orthotopic LNCaP mouse models using contrast-enhanced ultrasound imaging. *Transl Cancer Res* 2021;**10**:3268-77.

61.Sindhwani S, Syed AM, Ngai J, Kingston BR, Maiorino L, Rothschild J, et al. The entry of nanoparticles into solid tumours. *Nat Mater* 2020;**19**:566-75.

62.Subhan MA, Yalamarty SSK, Filipczak N, Parveen F, Torchilin VP. Recent Advances in Tumor Targeting via EPR Effect for Cancer Treatment. *J Pers Med* 2021;**11**.

63.Hoffmann A, Oborn B, Moteabbed M, Yan S, Bortfeld T, Knopf A, et al. MR-guided proton therapy: a review and a preview. *Radiat Oncol* 2020;**15**:129.

763 **Figures and legends**

764

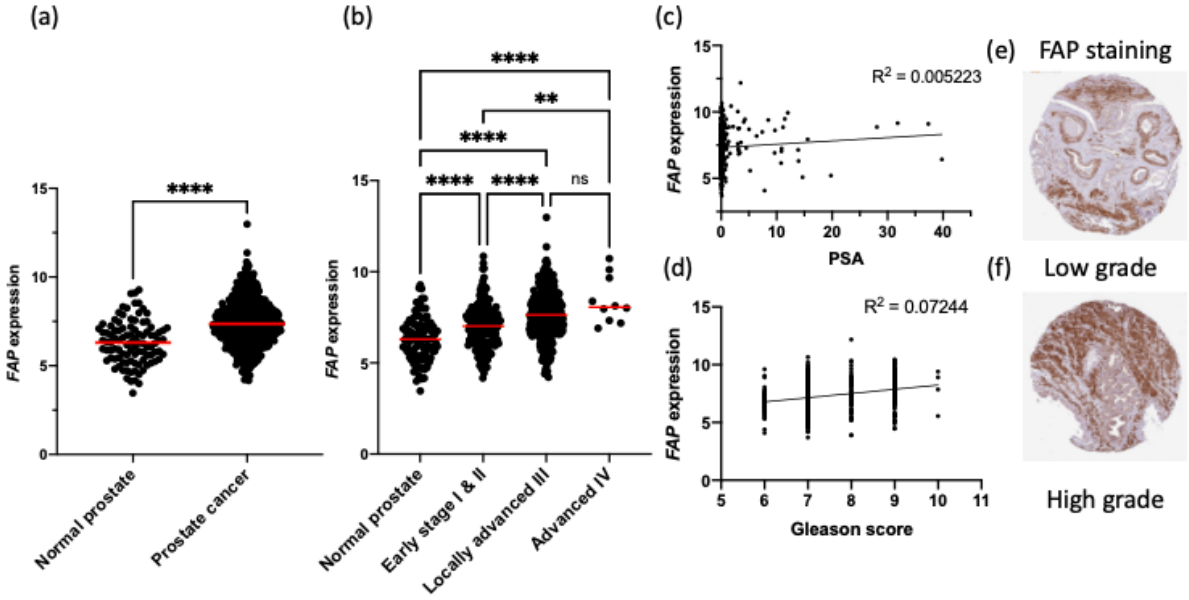

765
766
767

768 **Figure 1.** Transcriptomic analysis of *FAP* expression in clinical samples of prostate cancer. (a)
769 *FAP* gene expression values in prostate tumours compared with normal prostate obtained
770 from GTEX dataset. Red lines represent the medians of each group. (b) *FAP* expression in
771 relation to pathological T staging, (c) Gleason score and (d) PSA levels. (e) FAP
772 immunohistochemistry in biopsies of low grade and (f) high grade prostate adenocarcinoma
773 (images obtained from Human Protein Atlas).

774
775
776
777
778

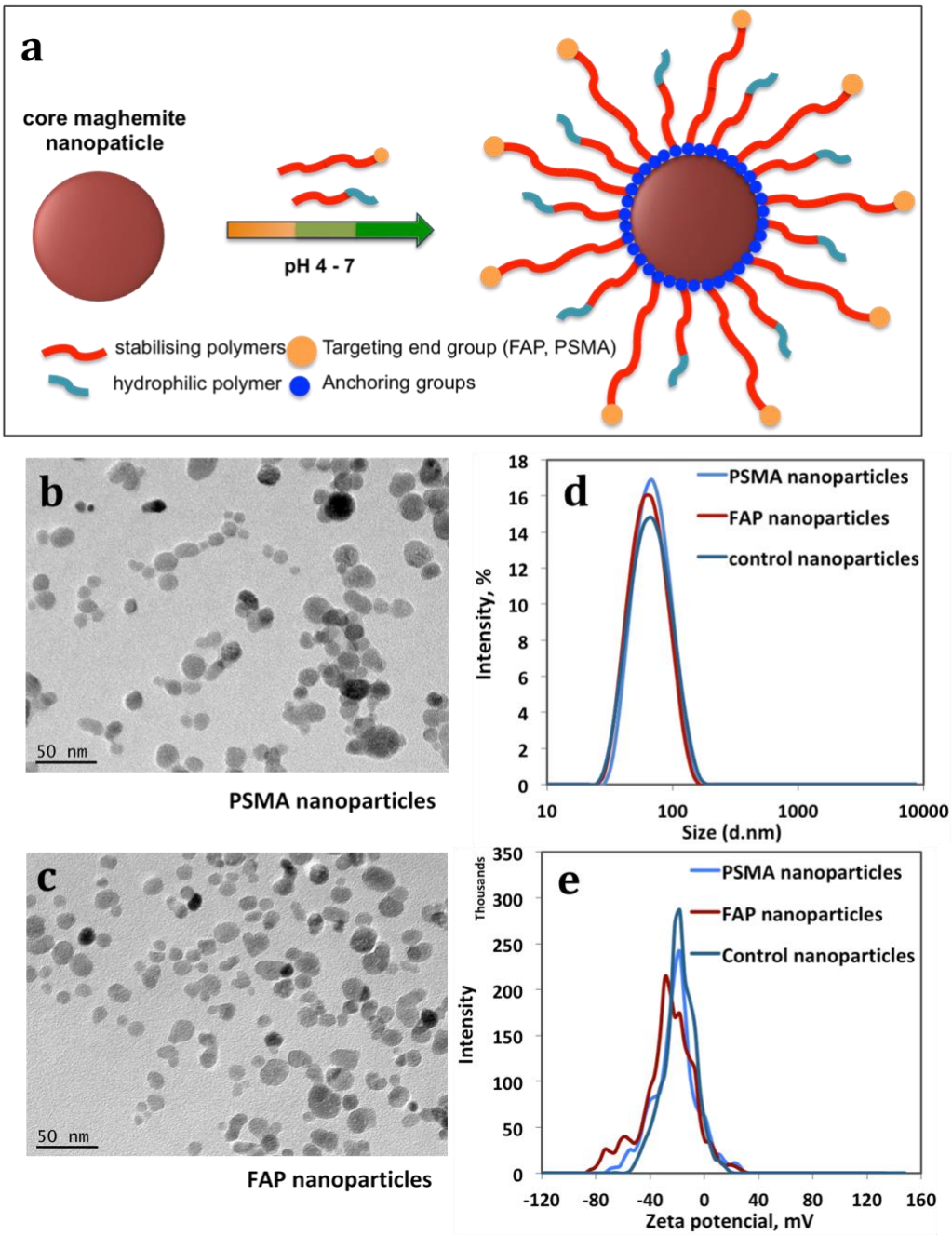

Figure 2. Preparation and characterization of FAP nanoparticles, PSMA nanoparticles and non-targeted control nanoparticles. (a) Schematic illustration of preparation of FAP/PSMA nanoparticles. (b, c) TEM images of FAP and PSMA nanoparticles at 60K x magnification. (d) Hydrodynamic size distribution by intensity and (e) zeta potentials of FAP and PSMA and unconjugated control nanoparticles measured by dynamic light scattering.

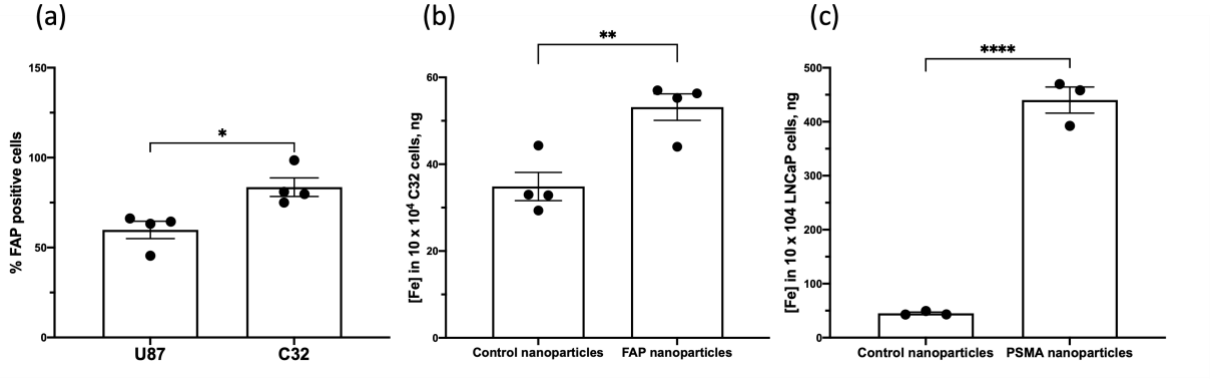

Figure 3. Evaluation of *in vitro* binding activity to cells expressing molecular PSMA and FAP targets. (a) Flow cytometric analysis of proportion of FAP-positive U87 and C32 cells. (b) Cellular uptake of PSMA nanoparticles and non-targeted nanoparticles in PSMA-positive LNCaP cells. (c) Cellular uptake of FAP nanoparticles and non-targeted nanoparticles in FAP-positive C32 cells. Data presented as mean ± SEM from 3-4 replicates per condition. PSMA vs non-targeted nanoparticles, $p<0.0001$, $t(4)= 16.306$, FAP vs non-targeted nanoparticles, $p< 0.0001$, $t(4)= 18.892$, independent sample test.

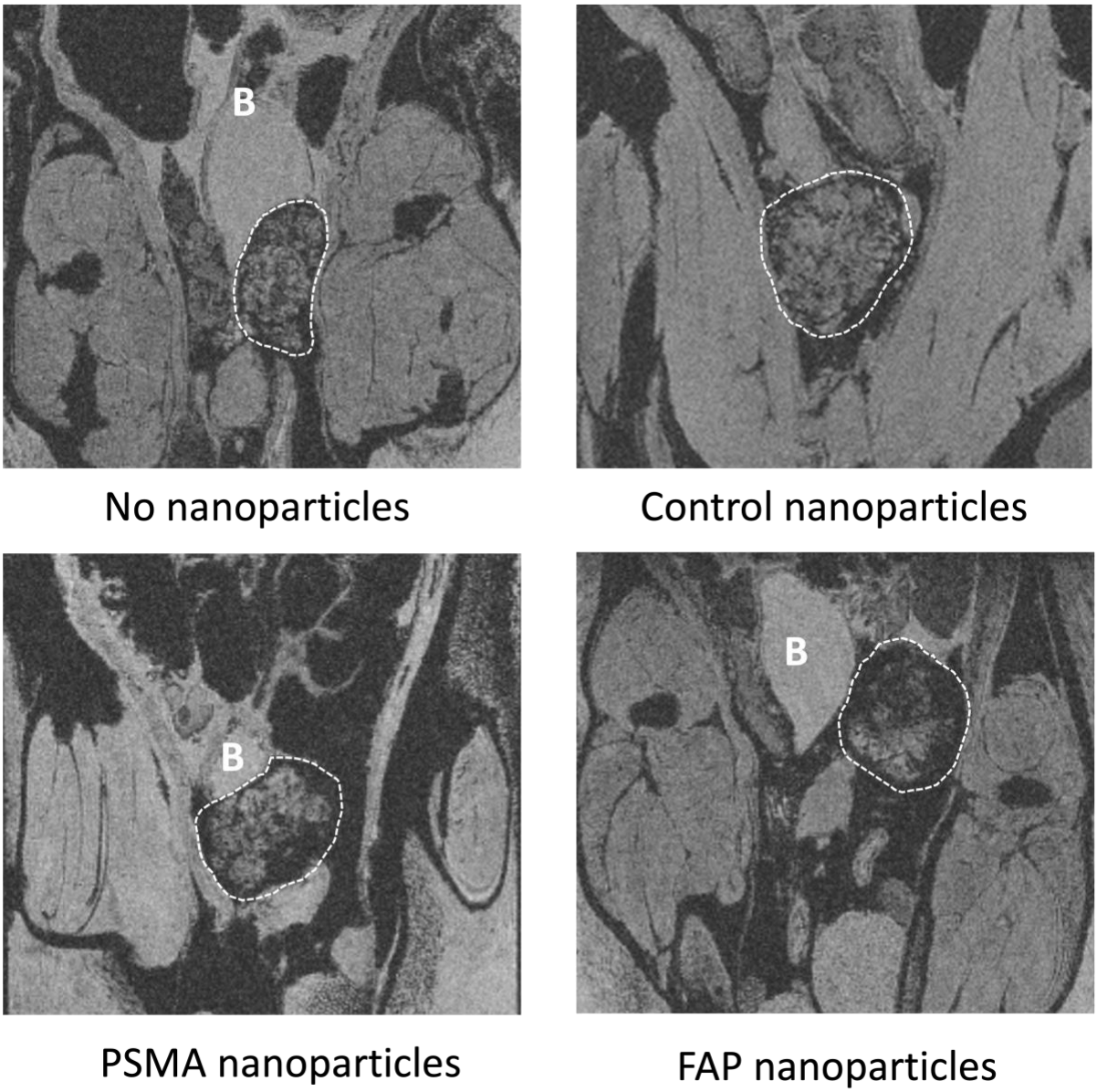

Figure 4. Representative coronal view of the lower abdomen in whole body T_2-W 16.4T MRI of mice bearing orthotopic prostate tumours 24 hours after intravenous injection with nanoparticles (40 mg Fe/kg) (representative images). PSMA nanoparticles and FAP nanoparticles enhance tumour contrast on MRI, relative to the administration of no nanoparticles and unconjugated control nanoparticles. B indicates bladder, white dotted border indicates orthotopic prostate tumour.

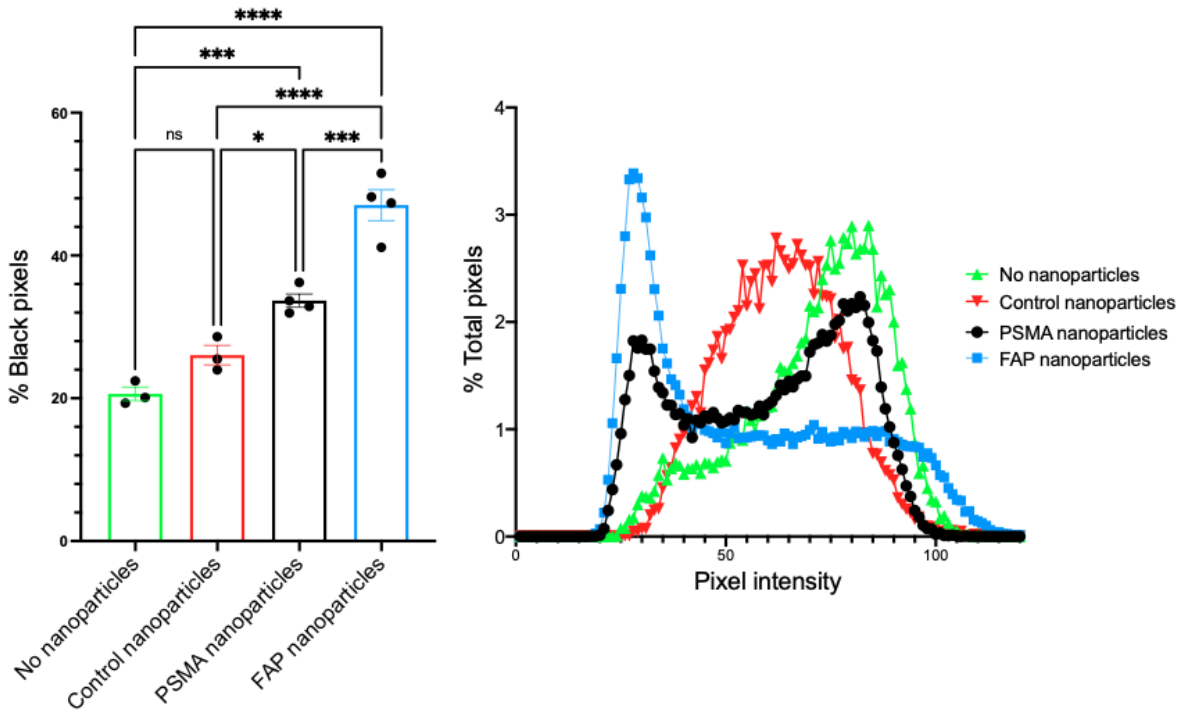

Figure 5. (a) Proportion of hypointense (black) pixels on T_2-W 16.4T MRI in murine orthotopic prostate tumours 24 hours after intravenous injection of FAP and PSMA nanoparticles (n=3-4 per group, data presented as mean ± SEM). (b) Representative total pixel distribution of analysed ROIs.

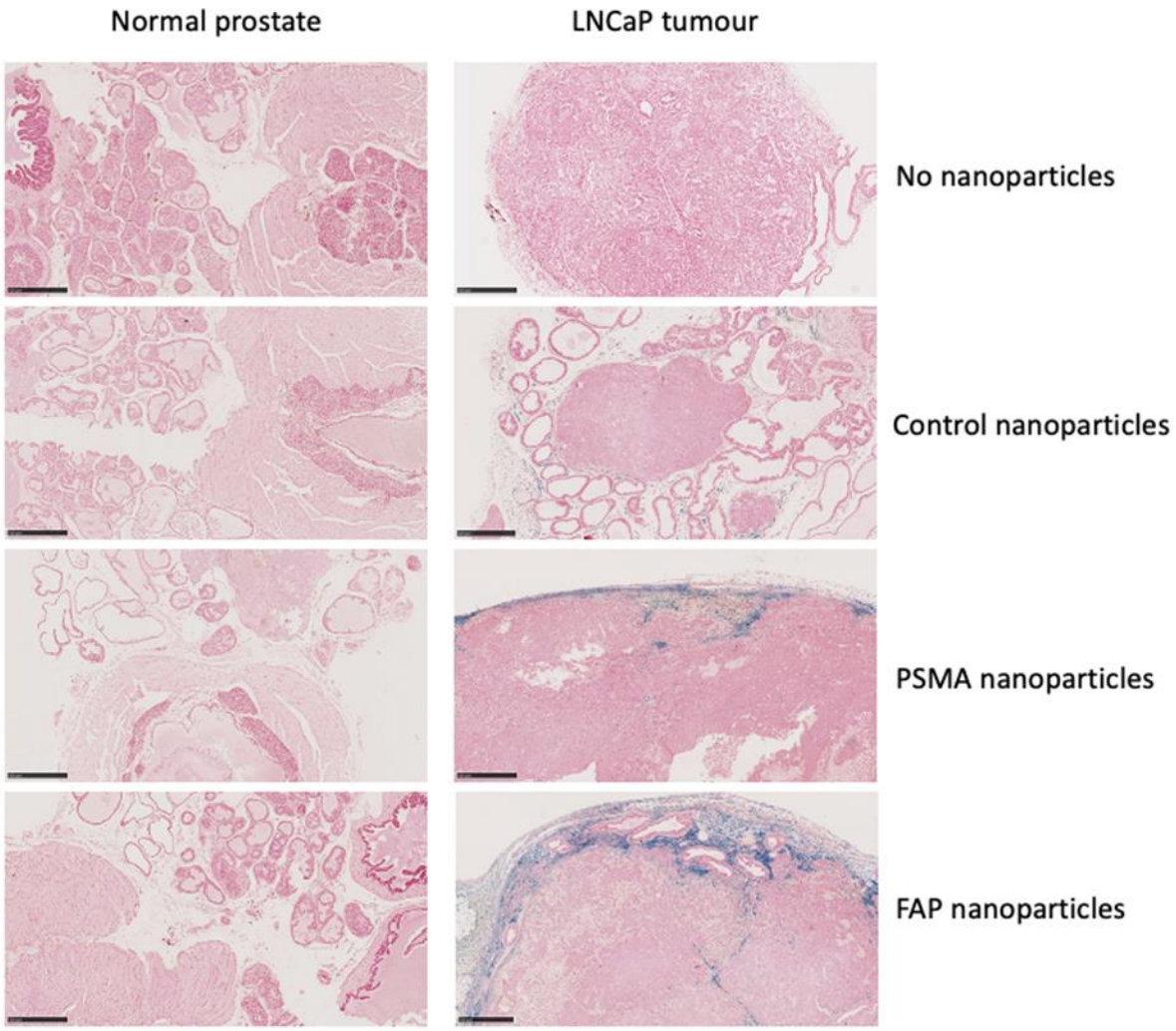

Figure 6. Representative images of Prussian blue staining of cross sections of normal prostates and orthotopic prostate tumours after intravenous injection with no nanoparticles, control nanoparticles, PSMA nanoparticles and FAP nanoparticles (all nanoparticles 40 mg Fe/kg). All images 5x magnification, scale bar is 500 µm.

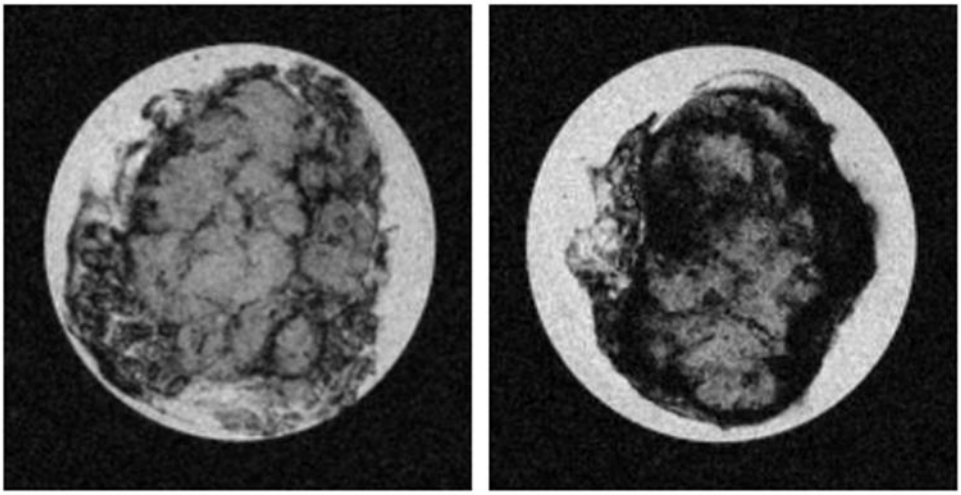

PSMA nanoparticles FAP nanoparticles

Figure 7. High resolution *ex vivo* T_2-W 11.7T MRI of murine LNCaP tumours 24 hours after intravenous injection of PSMA and FAP nanoparticles (representative image).

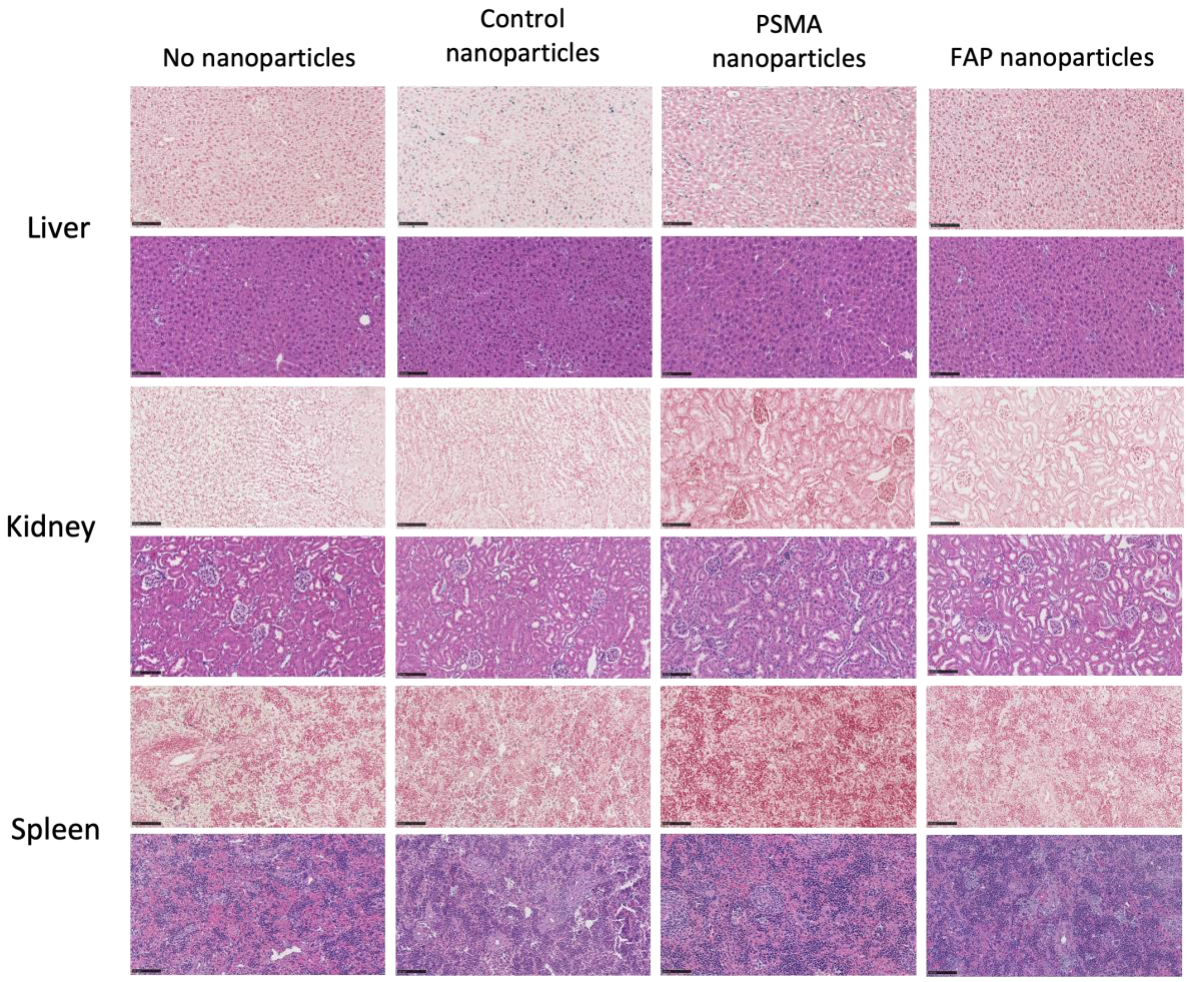

Figure 8. Haematoxylin and eosin (bottom row) and Prussian blue (top row) staining of liver, kidney and spleen of orthotopic LNCaP tumour mice, 24 hours after intravenous injection with nanoparticles. No changes in H&E staining were identified in the liver, kidney and spleen in all nanoparticle groups, compared to the no nanoparticle control. The kidneys and spleen did not show an increase in Prussian blue staining, relative to the no particle control, however a slight increase was observed in the liver, which was consistent across all nanoparticles. All images 20x, scale bar is 100 µm.